Sustainable **Energy & Fuels**



PAPER

View Article Online



Cite this: Sustainable Energy Fuels, 2022. 6. 3582

Received 28th February 2022 Accepted 14th June 2022

DOI: 10.1039/d2se00267a

rsc.li/sustainable-energy

Thermally fabricated cobalt telluride in nitrogenrich carbon dodecahedra as high-rate potassium and sodium ion battery anodes†

Debasish Sarkar, (10 ** Debanjan Das, (10 b) Sudhan Nagarajan (10 c) and David Mitlin (10 **d)

Cobalt telluride anchored to nitrogen-rich carbon dodecahedra (CoTe@NCD) was synthesized by simultaneous pyrolysis-tellurium melt impregnation of ZIF-67 MOFs. The purely thermal method involved no secondary chemicals and no waste byproducts. The result is a microstructure consisting of nanoscale 86 wt% CoTe intermetallic nanoparticles contained within a thin N-rich carbon matrix. During electrochemical cycling, the 21 nm average diameter CoTe provides short diffusion paths for Na⁺/K⁺ ions, which in conjunction with the electrically conducting carbon matrix allow for rapid potassiation or sodiation. As potassium ion battery (PIB and KIB) and sodium ion battery (NIB and SIB) anodes, CoTe@NCD demonstrates attractive reversible capacity, promising cycling stability, and state-of-the-art rate performance. For example, as a KIB anode, the CoTe@NCD electrode exhibits a reversible capacity of 380 mA h g^{-1} at 50 mA g^{-1} and a fast charge capacity of 136 mA h g^{-1} at 1000 mA g^{-1} . As a NIB anode, it also displays excellent rate capability achieving 620 mA h g^{-1} at 50 mA g^{-1} and 345 mA h g^{-1} at 1000 mA g^{-1} .

Introduction

The advent of rechargeable lithium-ion batteries (LIBs) revolutionized the field of portable electronics and electric vehicles by virtue of their long cycling life and high energy density.1-4 However, even wider implementation of LIBs is undermined by the uneven geographical distribution and low natural abundance of lithium precursors. Sodium and potassium ion-based storage technologies may be an obvious complement to lithium considering the high natural abundance of both elements in various mineral forms.5-9 The major roadblock to both, however, is the significantly worse rate and cycling performance versus LIBs. The much larger size of K⁺ (1.38 Å) and Na⁺ (1.02 Å) versus Li⁺ (0.76 Å) results in sluggish kinetics during electrochemical processes, as well as in structural damage during repeated insertion-extraction.10-12 It is a significant challenge to find suitable electrodes that could withstand enormous volume changes caused by repeated potassiation and sodiation processes over extended cycling.13-17

Despite the serious and well-publicized geopolitical sourcing issues, cobalt-based materials have proven to be instrumental across various engineering fields including energy storage, catalysis and electrocatalysis, high temperature gas-turbine vanes and buckets.18-20 Co-based alloys are also used to produce artificial joints and other biomedical implants.21 For commercial LIBs, LCO and Co-rich NMC are among the successful cathode materials, with Co-free and Co-reduced alternatives to date being less competitive. 18,22 Cobalt-based chalcogenides are attracting scientific interest as potential anode materials in PIBs and SIBs. 10,23-25 Cobalt-based sulphides and selenides have already been investigated thoroughly as NIB and PIB anodes with intriguing performance.25,26 However, to date, there are only a limited number of existing studies focusing on tellurides. 3,23,24,27 Metallic Te has an ultrahigh theoretical volumetric capacity of 2621 mA h cm $^{-3}$ as a K-ion battery anode. ^{3,27,28} So far, Guo et al. achieved a K-ion capacity as high as 2493 mA h cm⁻³ with a Te/ porous carbon composite electrode,27 whereas a K-ion capacity of 2552 mA h cm⁻³ has been reported for a Te/CNT/rGO electrode by Sun et al.3 Although cobalt-based sulphides and selenides deliver higher specific capacity as compared to their telluride counterparts, tellurides are expected to show improved rate performance. This is due to tellurium's intrinsic electrical conductivity (2 \times 10² S m⁻¹) which far surpasses those of S (5 \times $10^{-16}~{\rm S~m}^{-1}$) and Se (1 $\times~10^{-11}~{\rm S~m}^{-1}$).^{27,28} In principle, this would also allow for greater utilization of the Te active material at fast charging rates, enabling for high power applications of batteries containing the element in one or both electrodes.

Prior approaches for synthesis of tellurides have been primarily wet chemistry based, achieving exciting results in the

^aDepartment of Physics, Malaviya National Institute of Technology Jaipur, Rajasthan-302017, India. E-mail: deb.sarkar1985@gmail.com; debasish.phy@mnit. ac.in

^bMaterials Research Centre, Indian Institute of Science, Bengaluru-560012, India ^cChemical & Biomolecular Engineering and Mechanical Engineering, Clarkson University, Potsdam, New York 13699, USA

^dMaterials Science and Engineering Program, Texas Materials Institute (TMI), The University of Texas at Austin, Austin, Texas-78712-1591, USA. E-mail: david. mitlin2@utexas.edu

[†] Electronic supplementary information (ESI) available. https://doi.org/10.1039/d2se00267a

final materials. Yang, Zou and co-workers employed a green phosphine-free synthesis procedure to obtain telluride nanocrystals with promising luminescence, photovoltaic and thermoelectric properties.29 Gupta et al. developed a solution-based colloidal synthesis method for fabrication of ferromagnetic Cr₂Te₃ and CuCr₂Te₄ nanocrystals with uniform morphology and narrow size distribution.30 Zhang et al. employed a lowtemperature (160 °C) hydrothermal method to synthesize graphene - supported cobalt telluride, opening an exciting new path for wet fabrication of various tellurides.23 The hydrothermal approach is particularly promising for syntheses because of its low environmental footprint, making this study seminal in the field. Kang and coauthors employed a spray pyrolysis method to yield cobalt telluride-carbon composite microspheres, achieving excellent K-ion storage performance with the materials.31 Recently, Kshetri et al. reported the synthesis of a MOF-derived CoTe@C porous composite on a Nifoam substrate through a facile wet-chemical method at room temperature.32,33 The composite demonstrated excellent performance as a supercapacitor electrode within both positive and negative voltage windows. The same group also prepared Co_{2-x}Fe_xP-N-C micropillar arrays on a Ni-foam substrate through the wet-chemical method and used it as an electrode in a high-performance solid-state supercapacitor device.34 The above studies illustrate the exciting range of wet chemistry based approaches that may be employed for fabricating nanostructured tellurides.

Here we fabricated cobalt telluride anchored to nitrogen-rich carbon dodecahedra (CoTe@NCD) by a facile one-step carbonization and Te melt infiltration of a cobalt-imidazolate framework (ZIF-67). ZIF-67 served as a single solid precursor for cobalt, nitrogen and carbon. A key point of novelty this approach has is that it involves no wet chemistry, byproducts, or waste materials. Simply ZIF-67 and Te were heat treated together in an inert high temperature (900 °C) environment. This work directly differentiates itself from all prior methods, which are chemistry rather than thermal approaches, involving a range of secondary chemicals. Since there is no waste and no intermediate chemistry, the thermal approach can be scaled up by increasing the volume of the inert furnace employed, in principle being suited for continuous ton-scale rotary kiln production where process temperatures near 1000 °C are routinely employed.35 NCD provides enhanced electrical conductivity and prevents deleterious aggregation of K and Na ion - active CoTe nanoparticles. The voids in NCD buffer the potassiation and sodiation - related volume expansion, while providing a secondary surface diffusion path for the ions. CoTe@NCD is demonstrated to yield promising performance as K and Na ion anodes, providing superior fast charge capability.

Experimental

Synthesis of CoTe@NCD

Cobalt-imidazolate framework (ZIF-67) nanocrystals were synthesized according to a previous report, albeit, without the addition of any surfactant.10 The as-synthesized ZIF-67s were then activated under vacuum at 100 °C for approximately 8 h.

The activated material was then ground with analytical grade tellurium powder in a 1:1 weight ratio in a glove box, followed by annealing at 900 °C for 2 h under an Ar atmosphere. This yielded the final CoTe@NCD product.

Analytical and electrochemical characterization techniques

The morphology, structure and composition of electrode materials were investigated using field emission scanning electron microscopy (FESEM) (FEI, Quanta FEG 650), transmission electron microscopy (TEM, FEI TECNAI G2 TF20ST) equipped with a high-angle annular dark-field (HAADF) imaging detector and an electron energy loss spectrometry (EELS) detector, X-ray diffraction (XRD, PANalytical Empyrean X-ray Diffractometer) and Raman spectroscopy (WITec, Nd:YAG laser with $\lambda = 532$ nm). The chemical states of different elements were analyzed using X-ray photo-electron spectroscopy (XPS) (AXIS ULTRA). The Brunauer-Emmett-Teller (BET) surface area and porosities for composite materials were measured using the N2 adsorption/desorption method. To determine the amount of carbon in the CoTe@NCD hybrid thermogravimetric analysis (TGA, METTLER TOLEDO) was performed in air at a heating rate of 5 $^{\circ}$ C min⁻¹.

All electrochemical tests were carried out using CR-2032 type coin cells in half-cell configuration. The working electrodes were prepared by casting a slurry of the active material (CoTe@NCD), carbon black and the polyvinylidene difluoride binder (8:1:1 in weight ratio) onto copper foil and drying out the solvent in a vacuum oven at 80 °C. The mass loading of the active material was about 1 mg cm⁻².

For the K-ion half-cell, an electrolyte of 0.8 M KPF₆ in ethylene carbonate (EC)/diethyl carbonate (DEC)/propylene carbonate (PC) (2:1:2 v/v/v) without any additives was used, along with potassium metal foil as counter and reference electrodes. In the Na-ion half-cell, Na-metal foil is used as both counter and reference electrodes, whereas the electrolyte consisted of 1 M NaClO₄ dissolved in EC: DEC with a volume ratio of 1:1. In both types of cell, glass fiber membranes (Whatman GF/D) were used as separators. Galvanostatic charge-discharge tests were performed on an Arbin battery cycler. The CV curves were recorded on a Princeton electrochemical workstation. All tests were conducted at room temperature.

Results and discussion

Morphological characterization of the as-synthesized ZIF-67, as shown in Fig. S1 (ESI†), reveals a rhombic dodecahedral shape with smooth faces and sharp edges. The XRD pattern and morphology of the mixture of ZIF-67 and Te powder are presented in Fig. S2.† The XRD pattern (Fig. S2a†) exhibits characteristic diffraction peaks of ZIF-67 and Te, confirming their high purity. Upon heating the mixture to 500-600 °C, the organic linkers (2-methylimidazole) decompose into nitrogen and cyano fragments, resulting in a local reducing atmosphere which reduces the Co²⁺ centers into metallic Co. During pyrolysis, the evolution of volatile species creates extensive porosity in the carbon host. The maximum pyrolysis temperature was

900 °C, which is low enough to allow for the retention of substantial nitrogen functionalities within the carbon. Tellurium melts at 449.5 °C, impregnating the carbon and reacting with the Co species to form a network of CoTe nanoparticles anchored to the walls.

Fig. 1a shows the Raman spectra of CoTe@NCD with two intense peaks at around 1354 and 1591 cm⁻¹ corresponding to the typical disorder-induced D band and in-plane vibration G band, respectively. The $I_{\rm D}/I_{\rm G}$ ratio of CoTe@NCD is 1.03, indicating that the carbon framework is highly disordered. The broad 2D peak centered at around 2786 cm⁻¹ indicates the presence of defective graphene planes within the carbon structure. 10,36 Fig. 1b shows the FESEM image of a collection of CoTe@NCD particles which highlights their roughened dodecahedron-shaped morphology, with a typical size in the 500 nm range. The CoTe@NCD particles retain the overall morphology of the ZIF-67 precursor, with the CoTe intermetallics being embedded in the carbon matrix. The relatively uniform shape and size distribution of the particles highlight the efficacy of the synthesis approach. As shown in Fig. S3[†]

the EDXS analysis confirms the presence of Co, Te, and N elements in the composite structure. The presence of N is due to the structural nitrogen in ZIF-67, which is partially retained. The adsorption-desorption isotherms CoTe@NCD are shown in Fig. 1c with the corresponding pore size distribution (PSD) obtained using Barrett-Joyner-Halenda (BJH) analysis being shown in the inset. The type IV isotherms along with the H3 hysteresis loop in the latter half part with $P/P_0 = 0.5$ –1.0 is quintessential for the mesoporous structure. The powder has a Brunauer-Emmett-Teller (BET) surface of 156.5 $\text{m}^2 \text{ g}^{-1}$ and a total pore volume of 0.2 $\text{cm}^3 \text{ g}^{-1}$. Pore size distribution measured using BJH analysis indicates the presence of both micropores and mesopores. Creation of micropores can be attributed to the outgassing during the pyrolysis process, the volatile species being generated by the decomposition of the organic linkers. Some mesopores are generated by the outgassing, but they also pre-exist in the ZIF-67 precursor. In the XRD pattern shown in Fig. 1d, sharp Bragg reflections are indexed as hexagonal CoTe intermetallic (JCPDS card no. 034-0420).

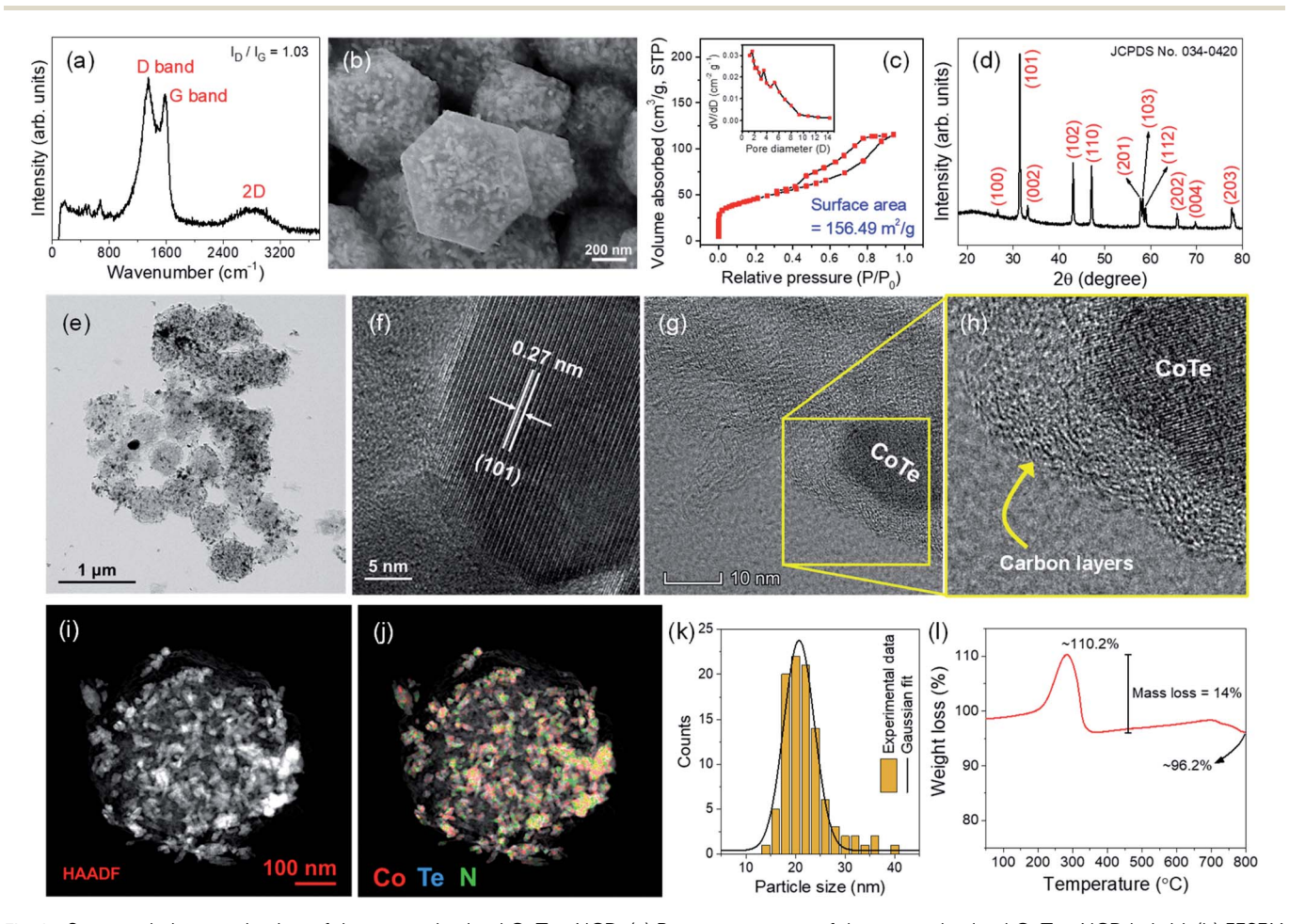


Fig. 1 Structural characterization of the as-synthesized CoTe@NCD. (a) Raman spectrum of the as-synthesized CoTe@NCD hybrid. (b) FESEM image of a collection of particles. (c) N₂ adsorption-desorption data of the powder; the inset shows corresponding pore size distribution (PSD) obtained using Barrett-Joyner-Halenda (BJH) analysis; (d) XRD pattern of the powder; (e) – (h) TEM and HRTEM images of carbon encapsulated CoTe nanocrystals. (i) and (j) HAADF-STEM image and associated EELS maps of a single particle. (k) CoTe intermetallic particle size distribution derived from a number of TEM images. (I) Thermogravimetric analysis (TGA) of CoTe@NCD powder performed in air.

Fig. 1e and S4† display the TEM images of CoTe@NCD, further highlighting the relatively uniform size distribution of NCD hosts and the CoTe intermetallics embedded inside. Fig. 1f shows the HRTEM image of a single CoTe intermetallic, highlighting that it is a single crystal. The fringes with an interlayer separation of ~ 0.27 nm correspond to the (101) crystal planes of hexagonal CoTe. The architecture of a single CoTe@NCD is an assembly of CoTe intermetallic nanocrystallites encapsulated within a highly defective carbon network. The HRTEM images in Fig. 1f-h demonstrate the presence of a few layers of carbon around CoTe which are prone to be more defective due to their formation on the CoTe particles and hence the seemingly amorphous nature. A detailed analysis of a number of the HRTEM images further suggest a low degree of ordering in the carbon material as depicted in Fig. 1g and h. Fig. 1i shows the HAADF contrast TEM image of a single CoTe@NCD, and Fig. 1j and S5† show the associated EELS maps of elemental Co, Te and N within the material, with Co and Te being associated together. The dense distribution of the CoTe intermetallics within the NCD host may be clearly observed from both analyses, the heavier Co and Te elements appearing white in the Z-contrast image. The size distribution of the CoTe intermetallics is shown in Fig. 1k, obtained after analyzing a number of bright field TEM images giving a mean value of 21 nm.

CoTe@NCD contains 14 wt% carbon, as per the thermogravimetric (TG) analysis result shown in Fig. 1l. In the TG curve of the CoTe@NCD powders, there is a gradual increase in weight as temperature increases after 130 °C and reaches 110.2% at 285 °C which can be attributed to the oxidation of CoTe to form cobalt oxide and tellurium oxide24 and/or cobalt tellurium oxide.37 Beyond this temperature, there is gradual mass loss, and at 800 °C, the total weight of the material stands at 96.2%. A net mass loss of 14% between 285 and 800 $^{\circ}\mathrm{C}$ can be ascribed to the decomposition of NCD.

XPS analysis was performed on CoTe@NCD. In Fig. S6a†, the survey spectrum shows the existence of C, N, Co and Te in the material. Deconvolution of the C 1s spectra (Fig. S6b†) indicates the presence of C-C/C=C bands (284.6 eV), C-O/C=N (285-286 eV), C=O/C-N (\sim 287 eV), and COOH (289–291 eV) in the carbon network.11,36 Deconvolution of the N 1s spectrum (Fig. 2a) reveals the presence of pyridinic-N (N-6), pyrrolic-N (N-5) and

quaternary-N (N-Q) peaks, centered at around 397.0 eV, 399.5 eV and 401.5 eV, respectively.36 The N content in the carbon framework is calculated to be \sim 10%. In Fig. 2b, the core-level XPS spectrum of Co 2p shows two major peaks at 780.7 and 796.2 eV, which correspond to the Co $2p_{3/2}$ and Co $2p_{1/2}$ states and in accordance with the reported binding energies of CoTe.38 Positions of the two satellite peaks are also associated with the intermetallics. As per Fig. 2c, Te 3d_{5/2} and 3d_{3/2} are centered at binding energies of 573.0 eV and 583.1 eV, also in agreement with ref. 38. Despite being stored in glove bags, some superficial oxidation of Te might have occurred during transfer of the specimen from the glove box to the XPS system. Two additional peaks observed at binding energies of 586 eV and 575.8 eV and represented by 'TeO2' account for the superficial oxidation.

Potassium ion storage performance of CoTe@NCD is shown in Fig. 3. Here we have used 0.8 M KPF₆ in EC/DEC/PC (2:1:2 v/v/v) as an electrolyte for the PIB test. In one of our recent publications, we employed 0.8 M KPF₆ in EC/DEC/PC electrolyte combination to improve passivation ability of the carbonate electrolyte on potassium metal anodes, and the electrolyte effectively passivated and demonstrated an efficient K metal plating/stripping reaction.39 With this motivation, we introduced the electrolyte combination to evaluate the performance of the CoTe@NCD electrode with improved passivation ability. Fig. 3a displays the initial five cyclic voltammetry (CV) curves for the CoTe@NCD electrode, tested at 0.1 mV s⁻¹ within the voltage range of 0.01-3 V. The broad reduction peak initiating near 0.75 V in the first potassiation cycle is attributed to the formation of the solid electrolyte interphase (SEI),13,14 occurring concurrently with the reaction of CoTe and K ions. At cycle 2 and afterwards, the single reduction peak initiates closer to 1.25 V and is largely complete by 0.75 V. The oxidation peak centered at 1.8 V occurs at all cycles, including at cycle 1. Potassium redox mechanisms for other transition metal phosphides and tellurides have been studied, 10,23,24 and it is reasonable that the potassiation sequence for CoTe will follow an analogous path. The broad reduction peak is assigned to the formation of K_2 Te, according to the reaction CoTe + $2K^+$ + $2e^-$ → Co + K₂Te.^{23,24} The broad oxidation peak is associated with the decomposition of K₂Te and formation of metallic Te according to the reaction $K_2Te \rightarrow Te + 2K^+ + 2e^-$. This reversible reaction is the primary source of the capacity, since

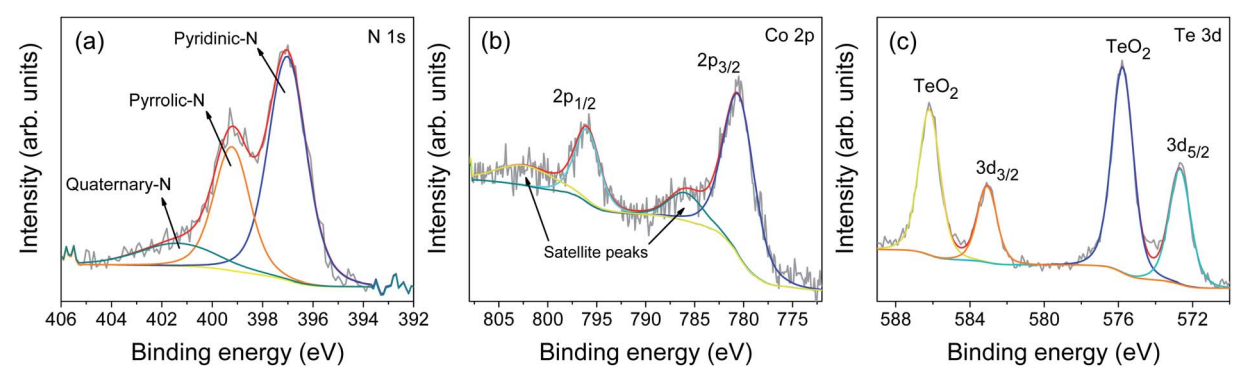


Fig. 2 Core-level high-resolution XPS spectra of (a) N 1s, (b) Co 2p, and (c) Te 3d, respectively, of the CoTe@NCD nanocomposite.

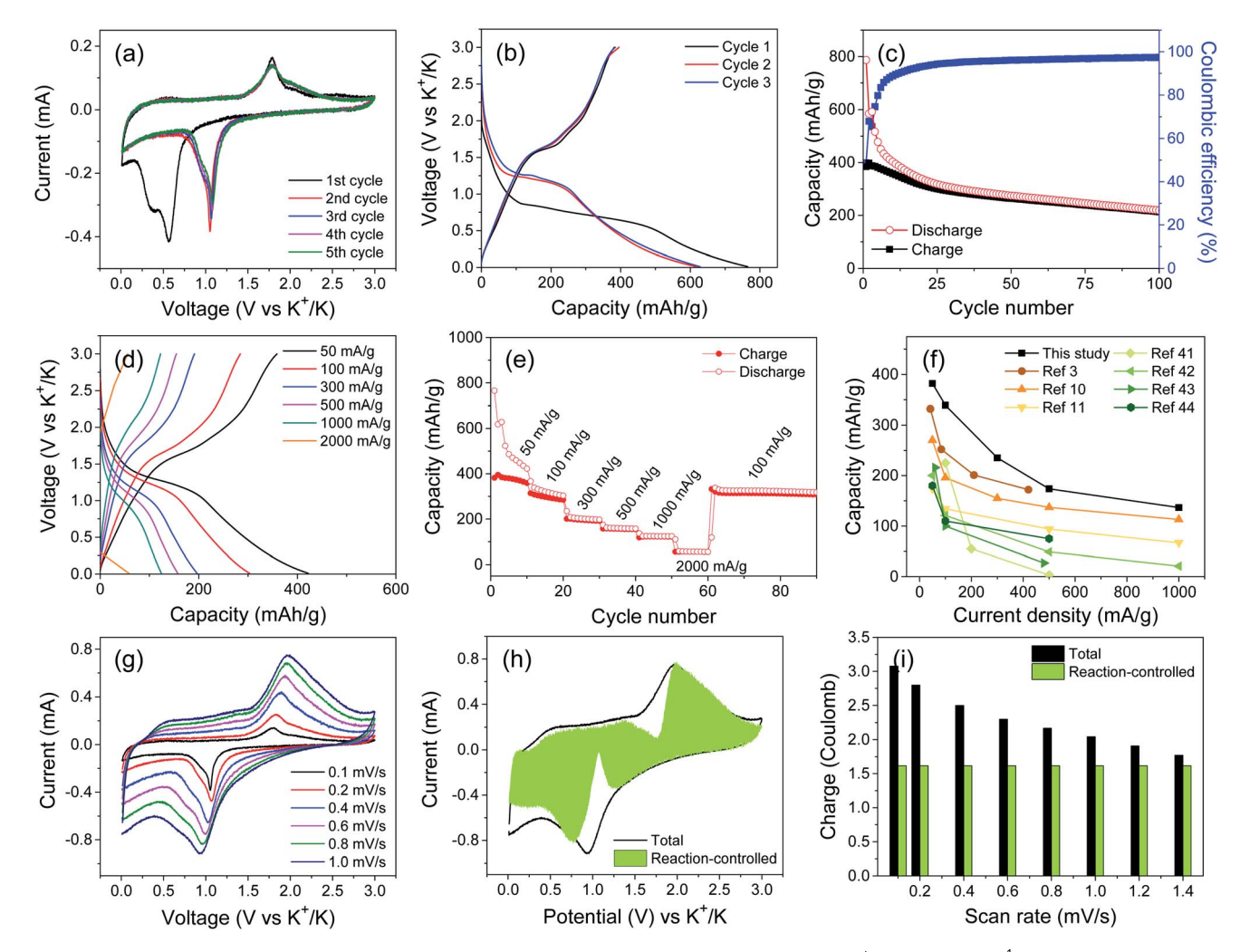


Fig. 3 Electrochemical analysis of CoTe@NCD as the PIB anode: (a) CV data within 0.01-3 V vs. K⁺/K, at 0.1 mV s⁻¹. (b) First few galvanostatic cycles at 50 mA g⁻¹. (c) Cycling performance at 50 mA g⁻¹. (d) and (e) Cycle 10 profiles at various current densities and the associated rate performance plot. (f) Rate performance comparison with state-of-the-art published PIB anodes. (g) CV at various scan rates for calculation of reaction kinetics. (h) Reaction-controlled current (shaded region) with respect to the total current obtained at a scan rate of $1\,\mathrm{mV}\,\mathrm{s}^{-1}$, and a (i) bar graph showing contribution from reaction-controlled processes towards the total charge stored at different scan rates.

the carbon host makes up only 14% of the total mass. Because of this low weight fraction of the carbon matrix, N-rich carbon is only a minor additional source of reversible K and Na storage capacity. This capacity derives from reversible adsorption at chemical and structural defect sites. 13,14,17,40 Nitrogen doping also enhances the electrical conductivity of carbon, which will improve the rate capability of the electrode. 10,11,40 Metallic Co is not K active, and the CoTe intermetallic should not re-form upon depotassiation. There are no literature reports of crystalline intermetallic re-formation after potassiation or sodiation. From the second cycle onwards, the redox peaks nearly overlap, indicating stable potassiated and depotassiated microstructures. During cycling, the metallic Co will have a dual role of stabilizing the Te phase from coarsening and agglomerating, while also aiding in the overall electrical conductivity of the electrode. It may be argued that synergy of N-rich carbon and Co is what allows such promising fast charge performance with both K and Na ions.

The steady-state cycling behavior is highlighted by the galvanostatic charge-discharge results shown in Fig. 3b for electrodes tested at 50 mA g⁻¹. For this current density, the steady state potassiation voltage plateau is located around 1.25 V. The steady-state plateau is due to the reversible formation of K2Te. The electrode delivers first depotassiation/potassiation capacities of 765.4/382 mA h g^{-1} . This affords an initial coulombic efficiency (ICE) of 50%, consistent with prior reports where ICE values ranging between 20 and 59% have been reported for Kbased nanostructured conversion systems.3,10,11,17 The irreversible capacities in the first few cycles are mainly attributed to the formation of the SEI layer. Moreover, at cycle 1, some damage is expected for the CoTe@NCD microstructure, providing an additional source of CE loss in addition to the SEI formation. After ten charge/discharge cycles, the CE value is above 85%, being over 99% during steady-state cycling.

As shown in Fig. 3c, when tested at 50 mA g^{-1} , the CoTe@NCD electrode shows good cycling stability. The early cycling capacity fade agrees with the prior literature reports and appears to be a general feature of potassiated (and sodiated) conversion anodes.3,10 After 100 cycles, the reversible capacity is 213 mA h g⁻¹ with a CE approaching 99%. According to Fig.-S7a† the capacity fade is associated with a shortening of the plateaus, indicating that less number of the conversion reaction sites is accessible. As per Table S1† cycling performance of CoTe@NCD compares well with that of prior reported PIB conversion anodes.3,10 Appreciable capacity fade, especially early in cycling, is a general feature of conversion electrodes with both K and Na due to associated large volume changes. 1,2,13 For the transformation of Te into K₂Te and Na₂Te, the volume changes are 155% and 115% respectively. The cycling stability of CoTe@NCD is unusually stable given that it contains only 14% carbon to buffer the expansion.

The rate performance of CoTe@NCD was measured at current densities varying from 50-2000 mA g⁻¹, as shown in Fig. 3d and e. The CoTe@NCD electrode exhibits highly favorable specific capacities of 340, 208, 174, 136, and 58 mA h g^{-1} at current densities of 100, 300, 500, 1000, and 2000 mA g^{-1} , respectively. The steady-state CE remains at over 99% at higher currents, confirming high reversibility of the electrode material. After decreasing the current rate from 2000 mA g-1 back to 100 mA g⁻¹, the reversible capacity is 337 mA h g⁻¹, which is more than 99% of the capacity measured at this rate prior to fast charging. Fig. 3f and Table S2† provide a detailed comparison of the rate performance of CoTe@NCD versus state-of-the-art telluride-based, cobalt-based. and carbon-based anodes.3,10,11,41-44 It may be observed that the current system is among the most favorable in terms of fast charge characteristics. These fast charge results may be explained by the nanoscale of the carbon framework and the 21 nm average CoTe nanoparticles that are further refined by the irreversible decomposition to Co and Te at cycle 1. This results in short solid-state diffusion distances during potassiation and depotassiation processes.

As discussed, the storage capacity of the CoTe@NCD electrode is primarily due to the reversible reactions in CoTe nanocrystallites. Its relative contribution can be further estimated by subtracting the contribution of the nanocarbon from the total charge storage capacity. As per the report by Wang et al., 45 ZIF-67 derived N-doped porous carbon with a pyridinic N content of ~5.3 atomic% delivered a K-ion capacity of 473 mA h $\rm g^{-1}$ at a current density of 50 mA $\rm g^{-1}$. It's capacity was 186 mA h g^{-1} when the current was increased to 2000 mA g^{-1} . Considering these reported capacities and the weight fraction of NCD in the CoTe@NCD hybrid (14%), the capacity contribution from CoTe can be estimated to be 316, 292, 195, 138, 108 and 29 mA h g⁻¹ at current densities of 50, 100, 300, 500, 1000, and 2000 mA g⁻¹, respectively. These calculations are presented in Fig. S8a.†

To gain further insight on the storage process in CoTe@NCD, electrochemical reaction kinetics were analyzed using CV at different scan rates, as shown in Fig. 3g. The kinetics can be separated into reaction-controlled versus diffusion-controlled, with the relative contributions varying with the scan rate. The peak current (i) in a cyclic

voltammogram and scan rate (v) will obey the following mathematical relation: $i(V) = av^b$, where a and b are both adjustable parameters. A value of b = 1 corresponds to a reactioncontrolled process (commonly labelled as capacitivecontrolled), while b = 1/2 corresponds to a diffusioncontrolled process. The so-called capacitive-controlled process is not EDLC charge storage per se since an ion battery anode surface area is not sufficient, rather, b = 1 indicates a process that can be faradaic charge transfer and/or reversible ion adsorption at defect sites. When b = 1/2, the charge storage reaction is a diffusion-controlled mechanism, such as the classic lithium-ion intercalation process into graphite.

With increasing scan rate, the peaks in the CV curve exhibit increasing currents (i) and overpotentials. In Fig. S9,† the plot of $\log(i)$ vs. $\log(v)$ yields b values of 0.88 and 0.85 for anodic and cathodic currents, respectively, indicating that further mathematical analysis is required to segregate the charge storage kinetics into reaction-controlled (ν) and diffusion-controlled ($\nu^{1/2}$ ²) processes. Now, the current (i) in a cyclic voltammogram and scan rate (v) obeys the mathematical relation $i(V) = a_1 v + a_2 v^{1/2}$ ². ^{10,12,17,37,42,46} As per the equation, the fraction of current contributions from reaction-controlled and diffusioncontrolled processes could be segregated through defining the constants a_1 and a_2 . In Fig. 3h, the current contribution from reaction-controlled processes at a scan rate of 1 mV s⁻¹ is plotted against the total current obtained in CV at the same scan rate. The plot indicates the dominance of reaction-controlled processes over diffusion-controlled processes. The detailed analysis at other scan rates reveals that the fraction of reactioncontrolled contribution increases from 53% at 0.1 mV s⁻¹ to the maximum value of 91% at 1.4 mV s⁻¹. These results are plotted in Fig. 3i. The dominant reaction-controlled contribution at 1.4 mV s⁻¹ agrees with reports for other fast-charge systems. Such a feature would be beneficial for achieving fast charging in half cells and high power in full cells.

The performance of CoTe@NCD towards sodium ion storage was also investigated. Fig. 4a presents the initial five CV cycles at 0.1 mV s⁻¹. The broad reduction peak at around 0.65 V during the first sodiation cycle is related to SEI formation and the irreversible decomposition of CoTe to Na₂Te + Co.^{23,37,47} From the second cycle onwards, the reduction and oxidation peaks are centered around 1.15 V and 1.7 V, respectively. This can be ascribed to the reversible conversion reaction of Te to Na₂Te, with Co being inactive. 23,24,47 The nearly overlapping redox peaks from the second cycle onwards indicate stable sodiated and desodiated microstructures. In Fig. 4b, the galvanostatic data show a sodiation voltage plateau around 1.2 V, associated with the formation of Na₂Te. The electrode has an ICE of 57%, consistent with prior reports for sodiated conversion anodes.15,37,47,48

The cycling results are shown in Fig. 4c. The reversible capacity is as high as 335 mA h g^{-1} at a current density of 100 mA g⁻¹ after 200 cycles with a CE \sim 99%, corresponding to ~50% of the second cycle capacity, which compares well to state-of-the-art NIB conversion anodes (Table S3†). According to Fig. S7b,† the capacity fade is associated with shortening of the plateaus, indicating that less number of the conversion reaction

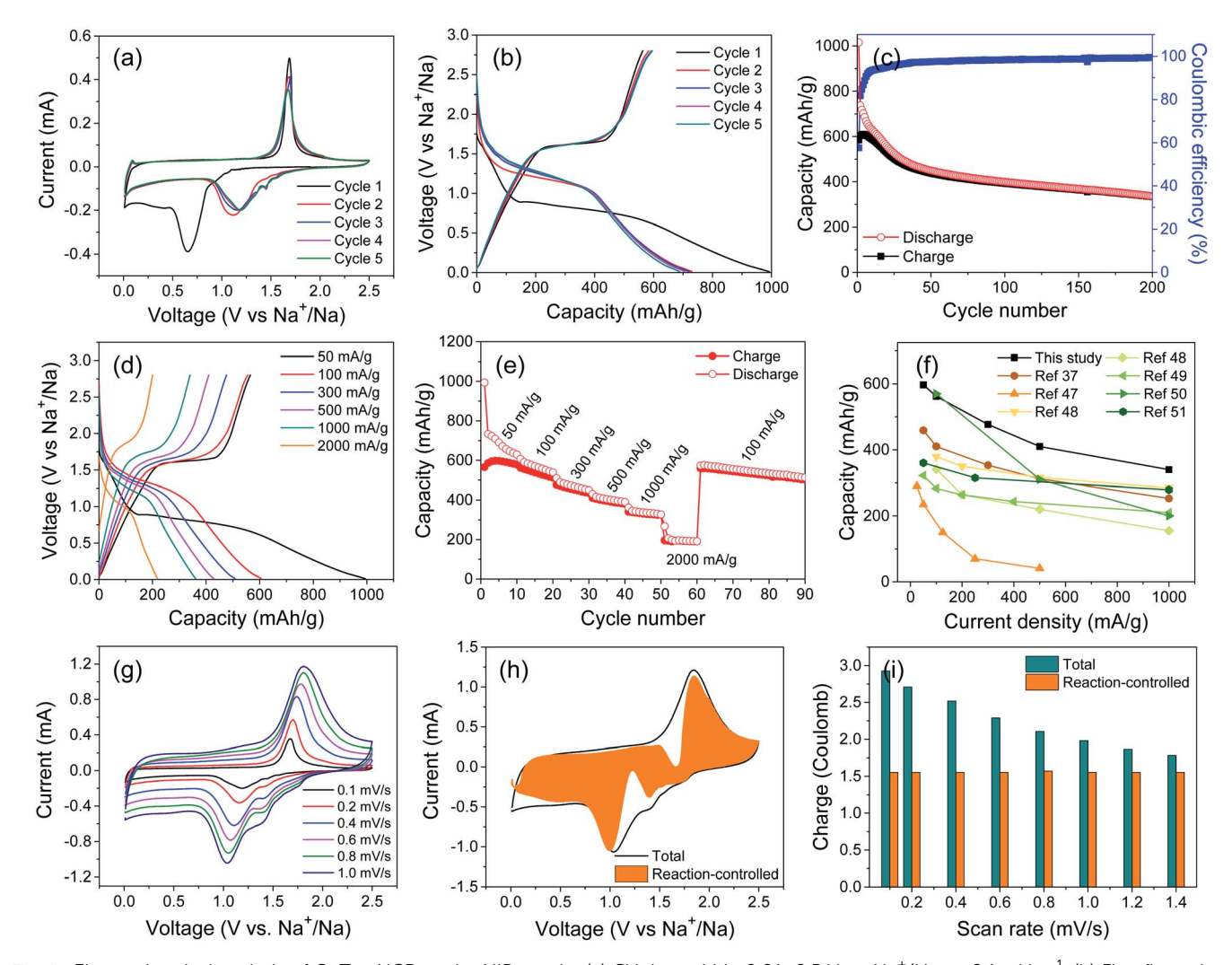


Fig. 4 Electrochemical analysis of CoTe@NCD as the NIB anode: (a) CV data within 0.01–2.5 V vs. Na⁺/Na, at 0.1 mV s⁻¹. (b) First five galvanostatic cycles at 50 mA g^{-1} . (c) Cycling performance at 100 mA g^{-1} . (d) and (e) Cycle 10 profiles at various current densities and the associated rate performance plot. (f) Rate performance comparison with state-of-the-art published NIB anodes. (g) CV curves at various scan rates for calculation of reaction kinetics. (h) Plot of reaction-controlled current (shaded region) with respect to the total current obtained at a scan rate of 1 mV s⁻¹, and (i) demonstration of reaction-controlled contribution towards total charge stored at different scan rates.

sites is accessible. In Fig. 4d and e, rate performance is displayed. At current densities of 50, 100, 300, 500, 1000, and 2000 mA g^{-1} , the reversible capacities are 620, 560, 490, 416, 345, and 207 mA h g^{-1} . This rate performance is state-of-the-art for conversion electrodes (Fig. 4f and Table S4†).5,23,24,37,47-51 When the current density is reduced back to 100 mA g^{-1} , a capacity of 559 mA h g⁻¹ is achieved. This is nearly the same capacity that was measured at this current before the fastcharging tests, indicating highly reversible fast charge behavior that does not damage the electrode.

It was also possible to estimate the capacity contribution of CoTe nanocrystallites towards the total Na-ion capacity in CoTe@NCD. For this calculation, the Na-ion capacity of ZIF-67 MOF derived porous carbon polyhedra with high-level nitrogendoping (10.2 atomic%) demonstrated by Zhao et al. was employed.⁵² The maximum Na-ion capacity of 249 mA h g⁻¹ was obtained at a current density of 50 mA g⁻¹, along with a retention of 145 mA h $\rm g^{-1}$ capacity at 1000 mA $\rm g^{-1}$. By considering the 14 wt% carbon content in the CoTe@NCD hybrid, the total Naion capacity due to CoTe nanocrystals is estimated to be 562, 532, 452, 387, and 320 mA h g^{-1} at current densities of 50, 100, 300, 500, and 1000 mA g^{-1} , respectively. The results are shown in Fig. S8b.†

Analysis of sodium-ion storage kinetics using CV at different scan rates is shown in Fig. 4g. In Fig. 4h, the plot of reactioncontrolled current with respect to the total current obtained at 1 mV s⁻¹ indicates that the reaction-controlled processes contribute 78% towards the total charge stored by the CoTe@NCD electrode. Similar analyses at different scan rates reveal dominance of the reaction-controlled contribution with progressively higher scan rates. As Fig. 4i indicates, the fraction of reaction-controlled contribution increases from 53% at 0.1 mV s⁻¹ to a value of 87% at 1.4 mV s⁻¹, indicative of fast charge/discharge characteristics.

In Table S5†, performance of CoTe@NCD as an anode material in KIB and NIB applications is compared. As per the above analyses, it is understandable that performance of the CoTe@NCD hybrid is far better towards Na-ion storage as compared to K-ion storage. Comparison of the CV curves (Fig. 3a and 4a) suggests reversible binding of K-ions occurring at higher voltages than for Na ions. Moreover, there is a larger hysteresis between anodic and cathodic peaks for K-ions (0.7 V) than that for Na-ions (0.6 V). Both the effects can be interpreted as the higher binding energy of active sites with the K ions than with the Na ions in addition to the smaller size of Na ions facilitating insertion/deinsertion processes in the electrode material followed by abundant redox reactions for charge storage. In both types of battery applications, the discharge curves are characterized by a high-voltage sloping region, a midvoltage plateau region followed by a low-voltage sloping region. However, comparing Fig. 3b and 4b, we argue that the Na-ion half-cell displays a much larger plateau region capacity (well over 200 mA h g⁻¹) as compared to the K-ion half-cell (\sim 130 mA h g⁻¹). The overall reversible capacity with K-ion is lower than that with the Na-ion (Table S5†). Moreover, the initial coulombic efficiency (ICE) for K is also lower, being at 50% versus 57% for Na, suggesting more irreversible K-ion trapping in CoTe@NCD. The reversible capacity of KIB decreases faster than that of NIB (as per Fig. 3e, f, and 4e, f), and the cycling performance is also found to be better in the case of

Conclusions

To summarize, unique CoTe nanoparticle grafted carbon dodecahedra are created through a one-step pyrolysis method with the ZIF-67 MOF and Te as precursors. Uniform dispersion of elemental Co in the MOF supports the growth of agglomeration free 21 nm CoTe nanoparticles. Both the porous carbon matrix and CoTe nanoparticles are highly active towards potassium and sodium ion storage. This enables the CoTe@NCD hybrid to deliver state-of-the-art reversible capacities as well as rate performance as compared to many other Co and Te based conversion-type KIB and NIB anodes.

Conflicts of interest

There are no conflicts to declare.

Acknowledgements

D. S. acknowledges financial support from Science & Engineering Research Board (SERB), Government of India, through the project SRG/2019/001211 and ISRO-RAC-S MNIT Jaipur through project RAC-S/PRO/21-22/02. D. M. (research co-conception and guidance; manuscript preparation) is supported by the National Science Foundation, CMMI, Div. of Civil. Mechanical, & Manufact. Inn., Award Number 1911905.

References

1 N. Yabuuchi, K. Kubota, M. Dahbi and S. Komaba, *Chem. Rev.*, 2014, 114, 11636–11682.

- 2 L. Li, Y. Zheng, S. Zhang, J. Yang, Z. Shao and Z. Guo, *Energy Environ. Sci.*, 2018, 11, 2310–2340.
- 3 Q. Liu, W. Deng and C.-F. Sun, *Energy Storage Mater.*, 2020, **28**, 10–16.
- 4 H. Zhang and Y. Qi, Sustainable Energy Fuels, 2022, 6, 954-970.
- 5 Z. Jian, Z. Xing, C. Bommier, Z. Li and X. Ji, Adv. Energy Mater., 2016, 6, 1501874.
- 6 G. He and L. F. Nazar, ACS Energy Lett., 2017, 2, 1122-1127.
- 7 J. Zhou, J. Chen, M. Chen, J. Wang, X. Liu, B. Wei, Z. Wang, J. Li, L. Gu, Q. Zhang, H. Wang and L. Guo, *Adv. Mater.*, 2019, 31, 1807874.
- 8 C. Yang, X. Sun, X. Zhang, J. Li, J. Ma, Y. Li, L. Xu, S. Liu, J. Yang, S. Fang, Q. Li, X. Yang, F. Pan, J. Lu and D. Yu, *Carbon*, 2021, 176, 242–252.
- 9 T. Yao, M. Yao and H. Wang, Sustainable Energy Fuels, 2022, 6, 822–833.
- 10 D. Das, D. Sarkar, S. Nagarajan and D. Mitlin, *Chem. Commun.*, 2020, 56, 14889–14892.
- 11 J. Bai, B. Xi, H. Mao, Y. Lin, X. Ma, J. Feng and S. Xiong, *Adv. Mater.*, 2018, **30**, 1802310.
- 12 Y. Ma, Y. Ma, H. Euchner, X. Liu, H. Zhang, B. Qin, D. Geiger, J. Biskupek, A. Carlsson, U. Kaiser, A. Groß, S. Indris, S. Passerini and D. Bresser, ACS Energy Lett., 2021, 6, 915–924.
- 13 T. Hosaka, K. Kubota, A. S. Hameed and S. Komaba, *Chem. Rev.*, 2020, **120**, 6358–6466.
- 14 C. Bommier, D. Mitlin and X. Ji, Prog. Mater. Sci., 2018, 97, 170–203.
- 15 L. Fan, X. Li, X. Song, N. Hu, D. Xiong, A. Koo and X. Sun, *ACS Appl. Mater. Interfaces*, 2018, **10**, 2637–2648.
- 16 J. M. Lee, G. Singh, W. Cha, S. Kim, J. Yi, S.-J. Hwang and A. Vinu, ACS Energy Lett., 2020, 5, 1939–1966.
- 17 W. Wei, H. Lv, X. Wang, W. Zhang, Z. Sun, J. Shi, M. Huang, S. Liu, Z. Shi and H. Wang, *Sustainable Energy Fuels*, 2022, 6, 1108–1120.
- 18 S. Qi, D. Wu, Y. Dong, J. Liao, C. W. Foster, C. O'Dwyer, Y. Feng, C. Liu and J. Ma, *Chem. Eng. J.*, 2019, 370, 185–207.
- 19 J. B. Gerken, J. G. McAlpin, J. Y. C. Chen, M. L. Rigsby, W. H. Casey, R. D. Britt and S. S. Stahl, *J. Am. Chem. Soc.*, 2011, 133, 14431–14442.
- 20 W. Zhang, L. Cui and J. Liu, J. Alloys Compd., 2020, 821, 153542.
- 21 Z. Zhou, Q. Wei, Q. Li, B. Jiang, Y. Chen and Y. Sun, *Mater. Sci. Eng.*, *C*, 2016, **69**, 46–51.
- 22 M. N. Obrovac and V. L. Chevrier, Chem. Rev., 2014, 114, 11444–11502.
- 23 G. Zhang, K. Liu and J. Zhou, J. Mater. Chem. A, 2018, 6, 6335-6343.
- 24 J. S. Cho, S. Y. Lee, J.-K. Lee and Y. C. Kang, *ACS Appl. Mater. Interfaces*, 2016, **8**, 21343–21349.
- 25 F. Han, C. Zhang, B. Sun, W. Tang, J. Yang and X. Li, *Carbon*, 2017, **118**, 731–742.
- 26 M. Wang, A. Peng, M. Zeng, L. Chen, X. Li, Z. Yang, J. Chen, B. Guo, Z. Ma and X. Li, Sustainable Energy Fuels, 2021, 5, 6381–6391.

- 27 S. Dong, D. Yu, J. Yang, L. Jiang, J. Wang, L. Cheng, Y. Zhou, H. Yue, H. Wang and L. Guo, Adv. Mater., 2020, 32, 1908027.
- 28 Y. Zhang, W. Lu, P. Zhao, M. H. Aboonasr Shiraz, D. Manaig, D. J. Freschi, Y. Liu and J. Liu, Carbon, 2021, 173, 11-21.
- 29 M. Wu, Y. Wang, H. Wang, H. Wang, Y. Sui, F. Du, X. Yang and B. Zou, Nanoscale, 2018, 10, 21928-21935.
- 30 K. Ramasamy, D. Mazumdar, R. D. Bennett and A. Gupta, Chem. Commun., 2012, 48, 5656-5658.
- 31 S. Yang, G. D. Park and Y. C. Kang, Appl. Surf. Sci., 2020, 529, 147140.
- 32 T. Kshetri, T. I. Singh, Y. S. Lee, D. D. Khumujam, N. H. Kim and J. H. Lee, Composites, Part B, 2021, 211, 108624.
- 33 T. I. Singh, G. Rajeshkhanna, S. B. Singh, T. Kshetri, N. H. Kim and J. H. Lee, ChemSusChem, 2019, 12, 4810-4823.
- 34 T. I. Singh, G. Rajeshkhanna, T. Kshetri, N. H. Kim and J. H. Lee, J. Mater. Chem. A, 2020, 8, 26158-26174.
- 35 W.-J. Liu, H. Jiang and H.-Q. Yu, Energy Environ. Sci., 2019, 12, 1751-1779.
- 36 H. Zhang, X. Xu, H. Wang, Y. Lyu, X. Liu, Y. Zhao, J. Shi, W. Liu, E. Paek and D. Mitlin, ACS Sustainable Chem. Eng., 2019, 7, 2867-2877.
- 37 Y. Ding, W. Wang, M. Bi, J. Guo and Z. Fang, Electrochim. Acta, 2019, 313, 331-340.
- 38 K. Wang, Z. Ye, C. Liu, D. Xi, C. Zhou, Z. Shi, H. Xia, G. Liu and G. Qiao, ACS Appl. Mater. Interfaces, 2016, 8, 2910-2916.
- 39 P. Liu, Y. Wang, Q. Gu, J. Nanda, J. Watt and D. Mitlin, Adv. Mater., 2020, 32, 1906735.

- 40 Z. Xie, J. Xia, D. Qiu, J. Wei, M. Li, F. Wang and R. Yang, Sustainable Energy Fuels, 2022, 6, 162-169.
- 41 C. Wang, B. Zhang, H. Xia, L. Cao, B. Luo, X. Fan, J. Zhang and X. Ou, Small, 2020, 16, 1905853.
- 42 M. Rashad, M. Asif, J. H. Shah, J. Li and I. Ahmed, Ceram. Int., 2020, 46, 8862-8868.
- 43 C. Fan, M. Zhao, C. Li, C. Wang, B. Cao, X. Chen, Y. Li and J. Li, Electrochim. Acta, 2017, 253, 333-338.
- 44 Z. Liu, K. Han, P. Li, W. Wang, D. He, Q. Tan, L. Wang, Y. Li, M. Qin and X. Qu, Nano-Micro Lett., 2019, 11, 96.
- 45 Y. Li, C. Yang, F. Zheng, X. Ou, Q. Pan, Y. Liu and G. Wang, J. Mater. Chem. A, 2018, 6, 17959-17966.
- 46 D. Sarkar, D. Das, S. Das, A. Kumar, S. Patil, K. K. Nanda, D. D. Sarma and A. Shukla, ACS Energy Lett., 2019, 4, 1602-
- 47 V. Ganesan, K.-H. Nam and C.-M. Park, ACS Appl. Energy Mater., 2020, 3, 4877-4887.
- 48 C. Wu, Y. Jiang, P. Kopold, P. A. van Aken, J. Maier and Y. Yu, Adv. Mater., 2016, 28, 7276-7283.
- 49 D. Zhou and L.-Z. Fan, J. Mater. Chem. A, 2018, 6, 2139-2147.
- 50 W.-J. Li, Q.-R. Yang, S.-L. Chou, J.-Z. Wang and H.-K. Liu, J. Power Sources, 2015, 294, 627-632.
- 51 J. Li, D. Yan, T. Lu, Y. Yao and L. Pan, Chem. Eng. J., 2017, 325, 14-24.
- 52 X. Gu, P. Dai, L. Li, J. Li, D. Li, H. Zhang and X. Zhao, ChemistrySelect, 2016, 1, 6442-6447.